

Full length article

A multi-scale correlative investigation of ductile fracture



M. Daly^a, T.L. Burnett^a, E.J. Pickering^{a,*}, O.C.G. Tuck^b, F. Léonard^{a,c}, R. Kelley^d,
P.J. Withers^a, A.H. Sherry^{a,b}

^a School of Materials, University of Manchester, Oxford Road, Manchester M13 9PL, UK

^b National Nuclear Laboratory, Chadwick House, Birchwood Park, Warrington WA3 6AE, UK

^c BAM Federal Institute for Materials Research and Testing, Unter den Eichen 87, 12205 Berlin, Germany

^d Thermo Fischer Scientific, 5350 NE Dawson Creek Drive, Hillsboro, OR 97124, USA

ARTICLE INFO

Article history:

Received 20 January 2017

Received in revised form

6 March 2017

Accepted 12 March 2017

Available online 16 March 2017

Keywords:

Gurson model

SA508

Correlative tomography

Void nucleation & growth

X-ray computed tomography

ABSTRACT

The use of novel multi-scale correlative methods, which involve the coordinated characterisation of matter across a range of length scales, are becoming of increasing value to materials scientists. Here, we describe for the first time how a multi-scale correlative approach can be used to investigate the nature of ductile fracture in metals. Specimens of a nuclear pressure vessel steel, SA508 Grade 3, are examined following ductile fracture using medium and high-resolution 3D X-ray computed tomography (CT) analyses, and a site-specific analysis using a dual beam plasma focused ion beam scanning electron microscope (PFIB-SEM). The methods are employed sequentially to characterise damage by void nucleation and growth in one volume of interest, allowing for the imaging of voids that ranged in size from less than 100 nm to over 100 μm . This enables the examination of voids initiated at carbide particles to be detected, as well as the large voids initiated at inclusions. We demonstrate that this multi-scale correlative approach is a powerful tool, which not only enhances our understanding of ductile failure through detailed characterisation of microstructure, but also provides quantitative information about the size, volume fractions and spatial distributions of voids that can be used to inform models of failure. It is found that the vast majority of large voids nucleated at MnS inclusions, and that the volume of a void varied according to the volume of its initiating inclusion raised to the power $3/2$. The most severe voiding was concentrated within 500 μm of the fracture surface, but measurable damage was found to extend to a depth of at least 3 mm. Microvoids associated with carbides (carbide-initiated voids) were found to be concentrated around larger inclusion-initiated voids at depths of at least 400 μm . Methods for quantifying X-ray CT void data are discussed, and a procedure for using this data to calibrate parameters in the Gurson-Tvergaard Needleman (GTN) model for ductile failure is also introduced.

© 2017 Acta Materialia Inc. Published by Elsevier Ltd. This is an open access article under the CC BY license (<http://creativecommons.org/licenses/by/4.0/>).

1. Introduction

The nucleation and growth of void damage in metals is critical to our understanding of many types of failure, for example in ductile fracture or high temperature creep. In such cases, the conventional approach has been to use destructive serial sectioning to quantify damage levels at various times on the path to ultimate failure. More recently, X-ray computed tomography (CT) has opened up the opportunity of studying void growth on a single sample over time [1,2], for example during simple tensile tests [3]. Unfortunately, the spatial resolution of X-ray CT means that either the defects must be

large or the samples small (the highest resolution achievable is approximately 1000th of the field of view using present 2000 pixel wide cameras [2]). This makes nucleation and growth difficult to study. In some cases, small cylinders of material have been extracted from specimens post-fracture and examined by CT to quantify void shapes, sizes, volume fractions, etc, at higher resolution [4,5]. Others have utilised laminography [6] or special sample geometries [7] to help control stress conditions in smaller samples subject to CT examinations. However, the use of X-ray CT on its own is limited, in that while it can image some defects, it is often of too poor a resolution to image smaller inclusions from which damage nucleates, or to capture the nucleation. Furthermore, grain boundaries and other microstructural features that may play an important role, for example in creep cavitation [8], are invisible to CT. In order to gain a fuller picture of failure correlative

* Corresponding author.

E-mail address: ed.pickering@manchester.ac.uk (E.J. Pickering).

approaches are required.

Multi-scale correlative imaging methods involve the characterisation of the features contained within a single volume of material across a wide range of length scales, using numerous complementary analytical techniques. They have been used, primarily in 2D, to great effect in the examination of structures in soft-tissue biological systems [9], and interest in their use in other areas of materials science is increasing rapidly. Recently, 3D correlative tomography methods have emerged [2], so that it is now possible to obtain multi-scale datasets even from challenging scenarios in which the volume of interest is hidden beneath the surface of a metallic sample [8,10]. In essence, high spatial resolution information from a volume of interest identified at lower resolution by X-ray computed tomography can be gathered using techniques such as focussed-ion beam serial sectioning, electron backscatter diffraction and transmission-electron microscopy. This information across all scales can be threaded together to generate a multiscale and multifaceted picture. Here, for the first time, we examine how the results of a 3D correlative approach can be used to provide greater insight into the mechanisms of ductile fracture.

The toughnesses of steels used in the construction of pressure vessels are of paramount importance, particularly when the components are critical to the safe operation of power plants. Historically, much attention has been devoted to the understanding of brittle fracture initiation and propagation in steels, and the associated ductile-to-brittle transition. However, there is now increasing interest in the ductile upper-shelf behaviour of pressure-vessel steels, since modern grades demonstrate such excellent start-of-life toughness that the onset of the brittle regime is less of a concern. It is well known that ductile tearing in steels proceeds through void nucleation, growth and coalescence. Large voids tend to nucleate and grow from inclusions in the microstructure (typically MnS, SiO₂ or Al₂O₃), and are joined together by sheets of smaller voids ('void sheets') nucleated at small particles such as carbides [11–14].¹ It is thought that the size and spatial distributions of voids, and their rate of growth, play a critical role in tearing behaviour. Equally, because it is assumed that the inclusions have no significant bond strength, they are often taken to represent the initial void population, meaning that their orientation and shape is also important [14,15].

In order to predict the ductile fracture behaviour of alloys, local mechanistic approaches like the Gurson-Tvergaard-Needleman (GTN) model are often utilised [16–19]. Derived from the original work of Gurson [16], with modifications by Tvergaard [17,18] and Needleman [19], the GTN model assumes that the material is homogeneous and behaves as a continuum. The voids are accounted for by influencing the global flow behaviour of the material and their effects on behaviour are averaged. Crucially, the model takes into consideration the dependence of yielding on the plastic strain and hydrostatic stress exerted on the material by introducing a strain softening term. This strain softening term accounts for the initiation, growth and coalescence of voids and is used in conjunction with the hardening of the matrix material which follows the Von Mises yield criterion. The model is defined by the following semi-empirical yield function, Φ :

$$\Phi(\sigma_e, \sigma_m, \bar{\sigma}, f^*) = \left(\frac{\sigma_e}{\bar{\sigma}}\right)^2 + 2q_1 f^* \cosh\left(\frac{3q_2 \sigma_m}{2\bar{\sigma}}\right) - (1 + q_3 f^{*2}) = 0 \quad (1)$$

where σ_e is the macroscopic von Mises stress, σ_m the macroscopic mean stress, and $\bar{\sigma}$ the flow stress for the matrix material. The constants q_1 , q_2 and q_3 were introduced by Tvergaard [17,18] to better reproduce experimental observations. The function f^* was introduced by Tvergaard and Needleman [19] to account for the rapid loss of stress carrying capacity (and failure) that accompanies void coalescence, which the original model by Gurson did not account for. f^* is defined in terms of the void volume fraction f as follows:

$$f^* = \begin{cases} f & \text{for } f \leq f_c \\ f_c + K(f - f_c) & \text{for } f > f_c \end{cases} \quad (2)$$

$$K = \frac{f_u^* - f_c}{f_F - f_c} \quad (3)$$

where f_c is the critical void volume fraction for void coalescence, f_F is the void volume fraction at final fracture, and f_u^* is ultimate value of f^* at final fracture, $f_u^* = 1/q_1$. The function for f^* when $f \leq f_c$ ensures that there is an acceleration towards the final volume fraction when f_c is exceeded. The value of f at the start of deformation is set as f_0 , the initial void volume fraction of the material. The change in f with an increment of deformation, denoted \dot{f} , is the sum of the volume fraction increase due to growth of existing voids and the increase due to the nucleation of new voids. The rate of void growth is assumed to be related to the plastic part of the strain rate tensor $\dot{\epsilon}_{ij}^p$, assuming the material is incompressible, whilst the void nucleation rate is related to the equivalent plastic strain rate $\dot{\epsilon}_{eq}^p$ [20]:

$$\dot{f} = \dot{f}_{\text{growth}} + \dot{f}_{\text{nucleation}} = (1 - f)\dot{\epsilon}_{ij}^p + \Lambda \dot{\epsilon}_{eq}^p \quad (4)$$

$$\Lambda = \frac{f_N}{s_N \sqrt{2\pi}} \exp \left[-\frac{1}{2} \left(\frac{\epsilon_{eq}^p - \epsilon_N}{s_N} \right)^2 \right] \quad (5)$$

where f_N is the volume fraction of void-nucleating particles, ϵ_N the mean value of strain, and s_N the standard deviation. Hence, the nucleation of voids follows a normal distribution in which 50% of void-nucleating particles are assumed to have nucleated a void at the mean strain of ϵ_N [20]. In summary, the primary parameters that require calibration in order to run a GTN simulation are the following: f_0 , f_c , f_F (that describe void growth and coalescence to failure), ϵ_N , s_N , f_N (that describe void nucleation), q_1 , q_2 , and q_3 (that characterise material plasticity). Since GTN models are solved using finite-element method (FEM) approaches, another parameter, the crack-tip mesh size L_C , must also be determined – this is essentially the dimension of which behaviour is averaged. The adequate calibration of all these parameters is not an easy task. Typically it is achieved iteratively, by estimating values using the results of previous studies, running a finite element analysis using these parameters, comparing the simulation results to experiment, and adjusting the parameters accordingly before repeating. As a result, 'optimised' parameter values often bear little relation to the physical quantities that they are supposed to represent [21–26]. In this paper, we describe an experimental multi-scale correlative method that is capable of quantifying the damage induced by ductile fracture. The approach enables the detailed characterisation of the

¹ In this paper, we adopt the following naming convention for voids, which helps to avoid potential confusion arising from only referring to their size: inclusion-initiated voids (IIVs), and carbide-initiated voids (CIVs), depending on their initiation site.

microstructure associated with fracture, such that the features initiating individual voids can be identified, and our mechanistic understanding of ductile failure improved. Furthermore, we discuss how this data can be used to set some of the GTN parameters. A previous study has attempted to do this before [4], but here we outline a procedure that is not influenced by any iterative FE modelling (the quantification methods used in Ref. [4] were also significantly different to this study). Ductile fracture specimens of SA508 Grade 3 pressure vessel steel [27] are examined using medium and high-resolution 3D X-ray CT analyses, followed by serial-sectioning of a volume of interest using a dual beam plasma focused ion beam scanning electron microscope (PFIB-SEM, hereafter referred to as PFIB) accompanied by electron back-scatter diffraction (EBSD) and energy-dispersive X-ray spectroscopy (EDX).

2. Experimental

2.1. Material

The material used throughout this study originated from a large SA508 Grade 3 [27] steel ring forging, which was in the quenched-and-tempered condition. The bulk chemical composition of the block is given in Table 1. Compact-tension specimens for fracture toughness testing were extracted from the forging in the longitudinal-transverse orientation. The compact-tension tests were performed according to the European Structural Integrity Society (ESIS) P2-92 [28] standard with dimensions of thickness, $B = 25$ mm, width, $W = 50$ mm and an initial crack length to specimen width ratio, $a/W = 0.53$. Specimens were 20% side-grooved following fatigue pre-cracking, and tested at 50 °C. Tests were performed using the multi-specimen method at 50 °C. Following testing, specimens were cooled in liquid nitrogen (−196 °C) and broken open so that the amount of ductile crack growth could be measured, and specimens extracted for X-ray CT.

2.2. Tomography sample preparation

In order to probe the distribution of voids with depth, cylindrical core-style samples for X-ray CT imaging were machined from below the fracture surface of one compact-tension specimen using electrical discharge machining (EDM) as shown in Fig. 1. The cores were approximately 0.5 mm in diameter and 35–40 mm in length, and were extracted at particular intervals away from the tip of the fatigue pre-crack, $x = 0.5, 1, 2, 3$ and 4 mm, see Fig. 1. They were extracted from the mid-plane of the specimen where the highest levels of constraint (stress triaxiality) were expected to prevail, thereby sampling material with the highest level of ductile tearing damage. The surfaces of the specimens were lightly polished to remove any scaling resulting from the EDM.

2.3. 3D X-ray tomography

The extracted core specimens were imaged from the fracture surface to 4 mm below it using a Nikon Metrology 225/320 kV Custom Bay system, see Fig. 1b. This *medium-resolution* scan was performed with a Mo target using a voltage of 80 kV. The data

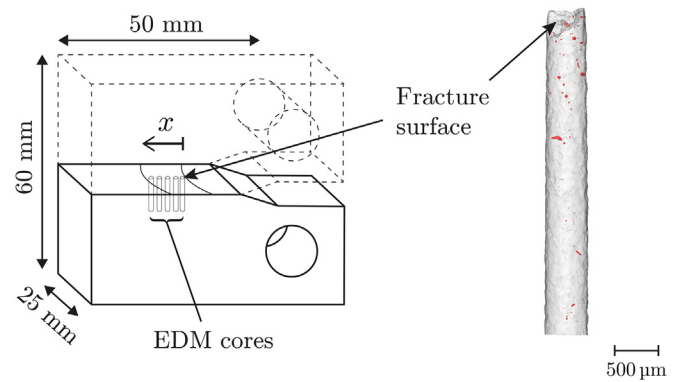


Fig. 1. Extraction of tomography cores from fractured compact tension specimens using EDM. (a) schematic of the compact-tension specimen and location of EDM cores (x measures the distance from the tip of the fatigue pre-crack). (b) Medium-resolution X-ray tomography image of extracted core. Voids (most probably inclusion-initiated voids, IIVs, given their size) are rendered in red. (For interpretation of the references to colour in this figure legend, the reader is referred to the web version of this article.)

acquisition was carried out with an exposure time of 1000 ms and no filtration. The number of projections was set to 3142 and the number of frames per projection was 1. The entire volume was reconstructed with a voxel size of $(2.0 \mu\text{m})^3$, giving an approximate resolution of 7–8 μm .

In addition to the medium-resolution scan at $(2.0 \mu\text{m})^3$ voxel size, a *high-resolution* scan was performed on a single EDM core of interest using a Zeiss Xradia Versa 500 3D X-ray tomography system, which produced images with an improved voxel size of $(0.8 \mu\text{m})^3$ (approximate resolution 2–3 μm) and greatly improved contrast. The scan was performed at a source voltage of 100 kV, and 1601 projections with an exposure time of 5 s at $\times 10$ magnification were taken.

Data processing was performed with Avizo® 9.0.0 software. An edge-preserving smoothing filter was applied to the raw data to reduce image noise in each data set. An edge-preserving smoothing filter was applied to the raw data to reduce image noise to help ensure the metal appeared as a single greyscale value. The core was then selected including the metal and all the internal voids to separate it from the background. A simple global greyscale threshold was used for this. From the voxels identified as the core a ‘top hat’ segmentation was applied to identify the voids inside the core. The ‘top hat’ approach was able to effectively deal with local variations in greyscale values of the matrix arising from changes in core diameter which were related to roughness and slight widening of the base of the core. Lastly several features identified as voids which came into contact with the metal surface had to be removed from the segmentation as they could have arisen from the EDM machining process. This was achieved by masking off the surface of the sample with the ‘paintbrush’ tool and interpolating across the height of the core. Fig. 2a and b compare the results of medium and high-resolution scans of the same area after segmentation.

The spatial coordinates and volumes of each void were extracted to quantify size and inter-particle spacing distributions. In order to manipulate the data usefully, the distance of each void from the fracture surface, Δz , had to be determined. There are a number of ways in which this could have been approximated: for instance, the contours of the fracture surface could have been extended to calculate the distance as shown in Fig. 3a. We decided to use a method which used the point at which the volume fraction metal present was = 0.5, Fig. 3b, since we felt this point was the best estimate of the centre of the crack path on average (and the material under the highest level of constraint). In order to measure

Table 1
Composition (wt%) of the SA508 Grade 3 steel examined.

C	Si	Mn	P	S	Cr	Mo
0.18	0.23	1.3	<0.005	<0.005	0.25	0.55
Ni	Al	Co	Cu	Sn	Ti	V
0.81	0.02	0.01	0.04	0.005	<0.001	0.01

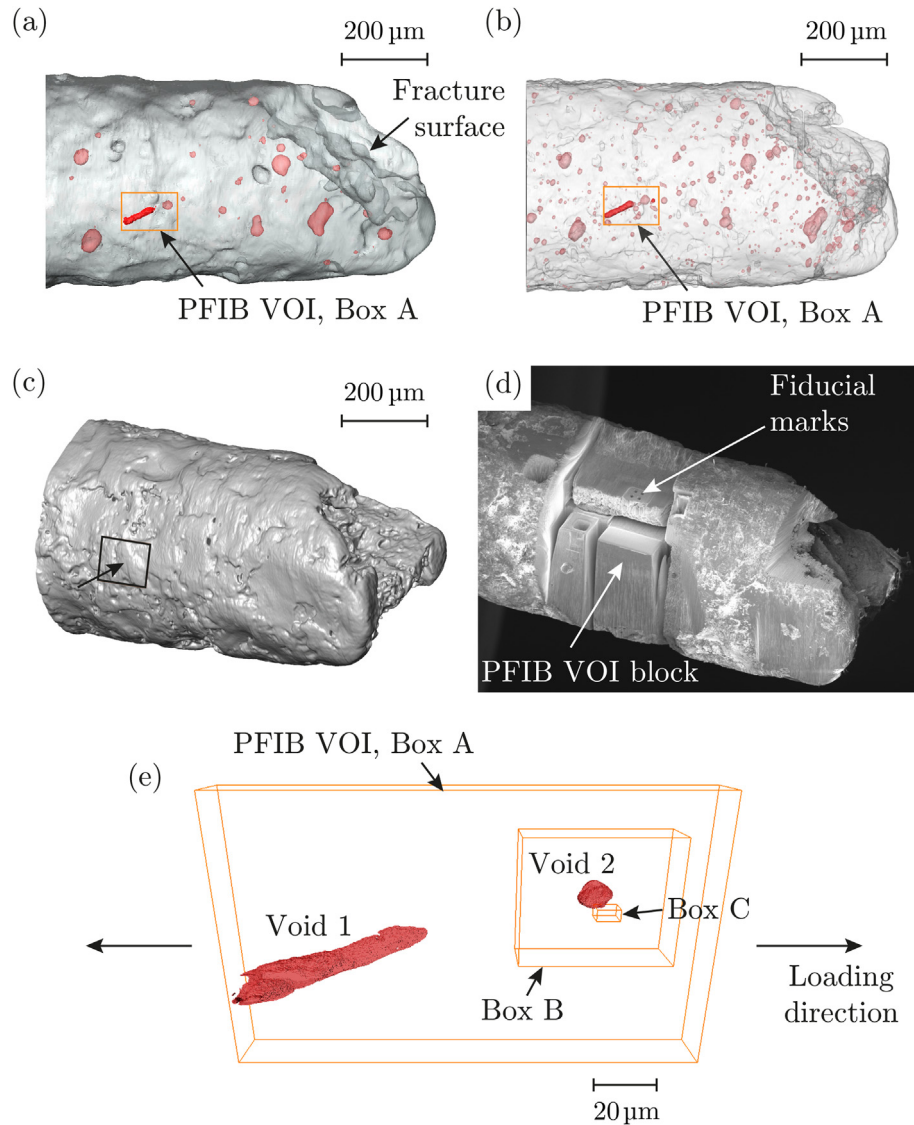


Fig. 2. (a) and (b) show a comparison of void populations measured using the medium-resolution and high-resolution scans, respectively. (c) shows a 3D reconstruction of the topology of the same specimen from the high-resolution results, onto which the VOI (marked with boxes in (a) and (b)) could be mapped. (d) shows the preparation of the PFIB region before sequential imaging (PFIB through lens detector image). (e) indicates the various sub-VOIs inside the full PFIB VOI. The full VOI, indicated in (a) and (b), is labelled Box A, with the sub-VOIs labelled Box B and Box C. The loading direction is indicated (left ↔ right).

void volume fraction (VVF), datasets were cut into voxel-thick slices and the areas of metal and void in each slice used to calculate the VVF. The fraction metal = 0.5 point was also found in this way by comparing the metal areas in slices intersecting the fracture surface to the average metal area in slices below the fracture surface. VVF values for slices above fraction metal = 0.5 were ignored, since their intersection with the fracture surface meant that measured VVFs were artificially low (voids that formed part of the fracture surface cannot be measured).

2.4. Plasma focused ion beam tomography

An FEI Helios dual-beam PFIB that utilises Xe^+ ions for milling and collects images through SEM [29] was used for high-resolution investigations of the microstructure of the sample. For the PFIB images, a volume of interest (VOI) was identified from the reconstructed high-resolution X-ray CT data, Fig. 2a–c. This region contained two voids of different geometries (marked in vivid red in

Fig. 2b), and lay approximately 600 μm below the fracture surface. 3D surface rendering of the high-resolution X-ray CT data was used to map the sub-surface VOI on to the surface of the specimen, and a strategy was designed by which a cross-section of the VOI could be prepared, Fig. 2c–d.

The VOI block shown in Fig. 2d was serially sectioned into 144 slices, each being 100 nm thick with a cross section block face $150 \times 115 \mu\text{m}$ in size. A rocking mill angle of $\pm 4^\circ$ was used to eliminate curtaining artefacts [29]. Electron beam images were collected at 2 kV, 800 pA using the through-lens detector (TLD) with a resolution of 6144×4096 pixels, giving a pixel size of 26 nm. The TLD signal was a mixed backscatter/secondary signal, giving clear crystallographic contrast. Each slice took approximately 380 s to record, principally due to the resolution of the imaging. Ion milling conditions were set at 30 kV and 59 nA, which provided the best balance of speed of milling and quality of the resultant surface.

The stack of serial sectioning images produced using the PFIB were aligned using the align slices module in Avizo[®] 9.0.0. A very

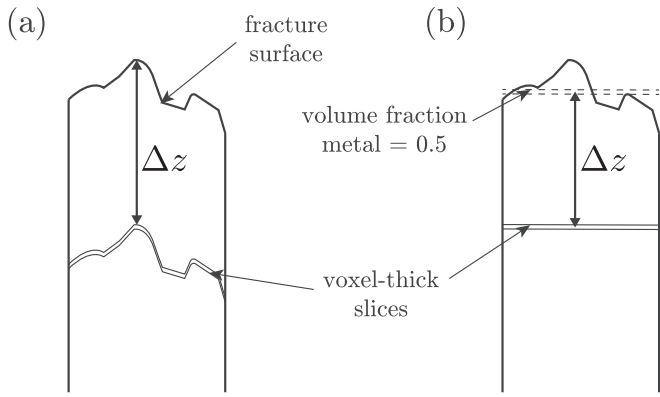


Fig. 3. Schematics of two possible procedures for estimating Δz , the distance to fracture surface (2D simplification). (a) extending the contours of the surface. (b) finding the location at which the fraction metal = 0.5 and using this as a reference. In both cases, voxel-thick slices are used to find VVFs and metal volume fractions as a function of Δz .

different approach for image filtering and segmentation was required for the PFIB data and was conducted as follows: the aligned images were filtered using the fast Fourier transform (FFT) filter to remove the light vertical curtaining effects produced from the Plasma FIB milling process. A sharpening filter was subsequently applied to compensate for some blurring resulting from the FFT filter. An edge-preserving filter and a median filter were applied to improve the definition of the voids, inclusions and carbides.

A 3D rendering of the surface of the core was created from the reconstructed X-ray CT data to allow direct comparison to the surface of the sample as imaged using the SEM. A basic appreciation of the sample orientation was refined by matching the topology between the two sets of images bringing the coordinates of the two datasets into registration. This allowed the sub-surfaces features observed in the X-ray CT datasets to be located with respect to the nearest surface and provided the information needed to prepare a site specific volume of interest using the PFIB. Finally, an additional edge-preserving filter and a bilateral filter were applied to reduce the noise and flatten the greyscale regions of the different metallic phases. The filters were chosen to give improved definition of the microvoids and carbides to aid this challenging segmentation. The segmentation process was further refined by performing an interactive threshold and a watershed treatment of the data to capture the voxels that corresponded to the majority of carbides and voids within the small sub-volume. Nevertheless, some shallow microvoids and some very small carbides could not be segmented. A more precise segmentation performed by hand was used on a very limited number of slices to render the interaction between microvoids and carbides.

3. Results

3.1. Microstructural characterisations

As shown in Fig. 2, the PFIB VOI (Box A) contained two voids of different geometries. These were labelled Void 1 (elongated void, $\approx 80 \mu\text{m}$ in length) and Void 2 (smaller, more spherical, $\approx 10 \mu\text{m}$ in size). Fig. 4 presents cross-sections of each of these voids, and compares the level of detail that was achievable using the three techniques: medium-resolution CT, high-resolution CT, and PFIB serial sectioning. The resolution achieved was influenced not only by the pixel size of the instrument used, but also by the contrast attained from the features imaged. The PFIB results provide direct evidence that the features assumed to be voids in the X-ray reconstructions were in fact voids, and not simply regions consisting

of a phase with a lower X-ray attenuation than the surrounding matrix.

The medium-resolution CT scan captures the larger Void 1, its location and approximate geometry, but does not adequately capture the smaller Void 2. The high-resolution scan captures significantly more detail in terms of the accuracy of the shape of both voids, but in addition it also reveals some indication of a second phase inside the void volumes of Void 1 and Void 2. Furthermore, it is clear that the absorption of this phase is intermediate between that of the metal matrix and the void. The single-slice PFIB-SEM data of Void 2 clearly shows that the phases contained within the voids are likely to be inclusions, consistent with results obtained by more traditional SEM analysis of the same material after grinding, polishing and etching, Fig. 5.

Fig. 6 shows all of the voids that were captured within the serial sectioned PFIB VOI volume (Box A), a total of 8 voids. All large voids found were associated with MnS inclusions, as identified by EDX, with the exception of Void 7, which appeared to be present on a grain boundary without an inclusion nearby. The PFIB analysis was also able to identify very fine voids, typically associated with small carbides (therefore labelled CIVs), which were found predominantly in close proximity to the large voids associated with MnS particles. The carbides and voids were distinguishable, despite possessing similar contrast, because a signal could be detected from the edges of voids and their appearance changed slice-by-slice – the electron signal returned from the edge of the void and the visibility of the back of the empty void varied. This was not the case with the carbide phase. In Fig. 7, PFIB images of these CIVs are compared to images obtained through standard SEM analysis. The difference in contrast of the carbides can be explained by the sample preparation and etching procedures: for Fig. 7a the material was PFIB milled and imaged using a through-the-lens detector which sampled both secondary and back-scattered electrons, whilst for Fig. 7b the material was etched with 2% nital solution and imaged in secondary-electron mode.

Fig. 8 shows the distribution of microvoids that were identified around Void 2 (Box B). The loading direction, which led to the ductile fracture of the sample, is indicated. There are clearly areas and directions in which these ‘satellite voids’ are more concentrated, perhaps in regions of concentrated shear stress, although it cannot be inferred at what point during failure (in particular, in relation to the growth of the large void) these microvoids formed. For a small region adjacent to Void 2 (Box C), Fig. 9, the carbides were separately identified and labelled in blue, (voids in red). As far as it was possible to tell, these small voids were always associated with the carbides in the microstructure. There was also some indication that the orientation of the strings of carbides was important for void nucleation – nucleation appeared more prevalent between those with long dimensions aligned parallel to the applied stress.

The final PFIB slice (the 144th) was imaged using electron back-scattered diffraction (EBSD) to observe the crystallography of the complex microstructure, Fig. 10. Voids 1 and 7 were the only voids that remained in the final PFIB slice. The EBSD map shows a region of strained material adjacent to Void 1, which was found to be populated by large numbers of CIVs (c.f. Fig. 8 for Void 2). The EBSD data also highlights the distinctive grain boundary where Void 7 is located and where a number of additional smaller voids have also been observed. The EBSD confirmed that Void 7 sat on a grain boundary, and it was the only one of the voids captured in the PFIB-SEM dataset that did not include a measurable inclusion.

3.2. Quantification of features

The void volume fraction (VVF) as a function of distance below the fracture surface is quantified in Fig. 11 using the medium-

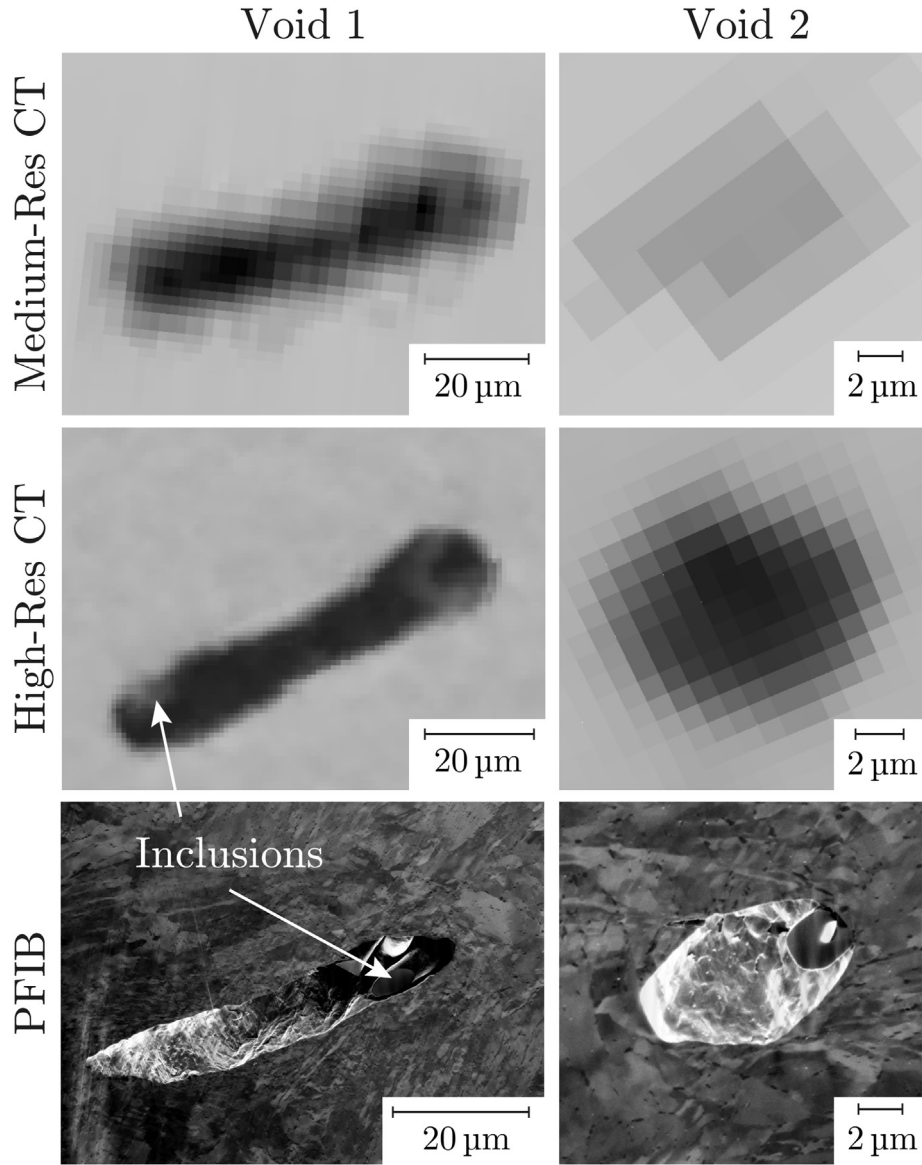


Fig. 4. Comparison of the void data obtained from the PFIB VOI (Box A) using the three tomography systems: the medium-resolution Nikon Custom Bay X-ray CT ($(2 \mu\text{m})^3$ voxel size), the high-resolution Versa 500 X-ray CT ($(0.8 \mu\text{m})^3$ voxel size) and the Plasma FIB serial section tomograph ($26 \times 26 \times 100 \text{ nm}^3$ voxel size resolution). Note that the inclusion found to the far left of Void 1 (seen in high-resolution X-ray CT data) was captured by the PFIB sectioning, but was not imaged in the particular slice shown here. The loading direction was left \leftrightarrow right in these images.

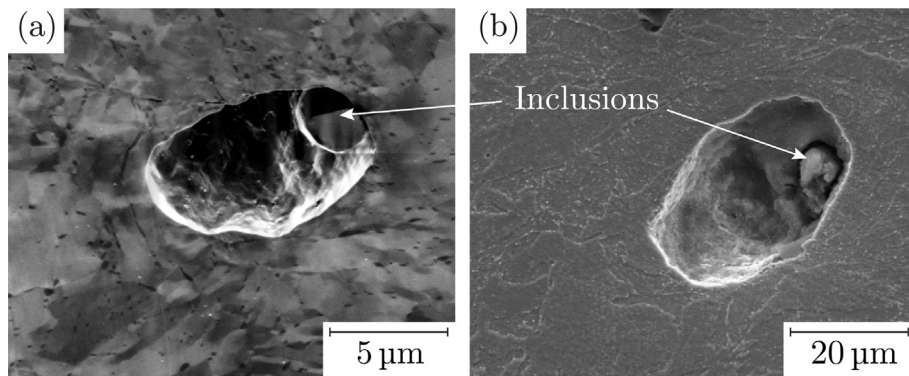


Fig. 5. Comparison between images of two different voids obtained from (a) PFIB imaging and (b) traditional 2D SEM imaging. The 2D SEM images were obtained from samples of the same compact-tension material prepared using standard metallographic techniques (etched in 2% nital), although here different regions are compared (in contrast to Fig. 4, which compares the same voids and inclusions). The loading direction was left \leftrightarrow right in (b).

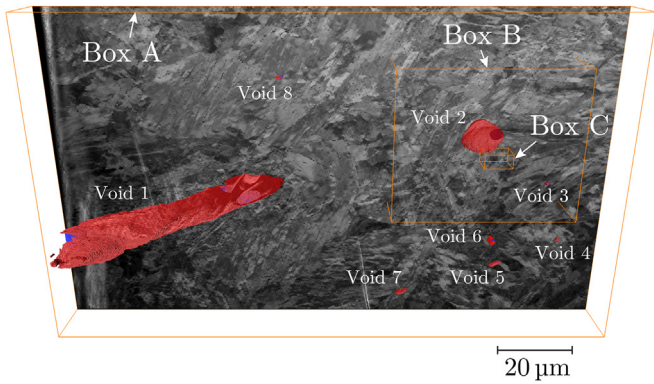


Fig. 6. A map of all large voids identified within the PFIB volume (Box A). The PFIB images also provide sufficient phase contrast to discern the complex microstructure of the ferritic steel. All voids are rendered in red, with inclusions rendered in blue. The loading direction was left ↔ right in this image. (For interpretation of the references to colour in this figure legend, the reader is referred to the web version of this article.)

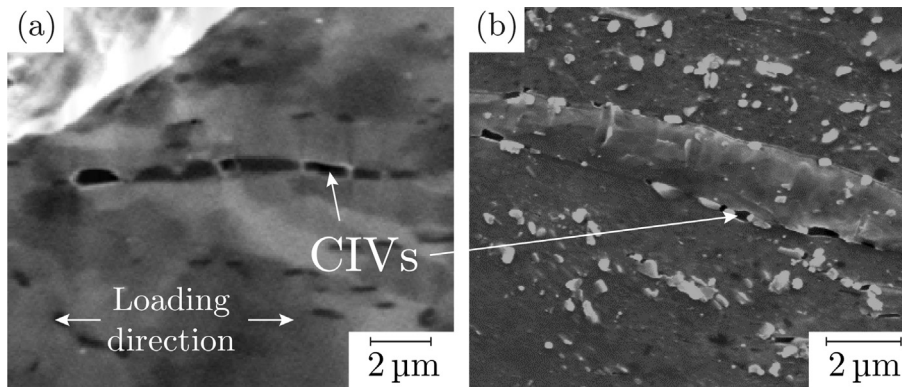


Fig. 7. Comparison between images of microvoids (CIVs) obtained from (a) PFIB imaging and (b) traditional 2D SEM imaging. The 2D SEM images were obtained from samples of the same compact-tension material prepared using standard metallographic techniques (etched in 2% nital).

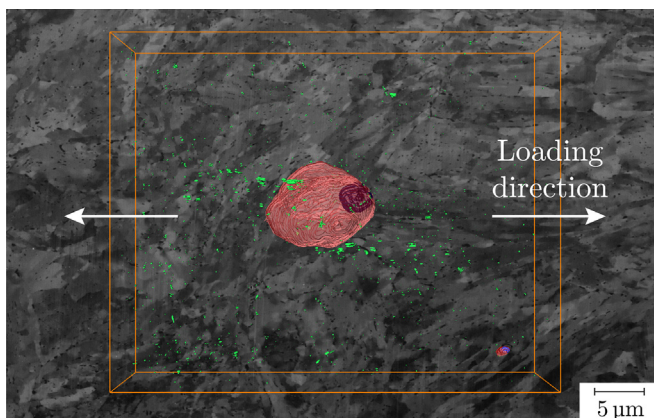


Fig. 8. Segmented volume of interest around Void 2 (Box B). IIVs are rendered in red, whilst CIVs are rendered in green. Inclusions are rendered in blue. An image of the final PFIB slice in the VOI is shown in black and white. (For interpretation of the references to colour in this figure legend, the reader is referred to the web version of this article.)

resolution CT data. The plotted line represents an average of the VVF distributions calculated in each of the five cores examined. The distance from the fracture surface is that measured to the point at which the volume fraction metal in the voxel-thick slices of X-ray CT data was equal to 0.5 (see Fig. 3b and associated discussion).

There is a sharp increase in the VVF within 500 μm of the fracture surface, peaking at $\text{VVF} \approx 0.018$, although some damage is present to depths of over 3 mm. The data presented for Δz values of less than 190 μm is plotted as a greyed line. This data should be viewed with caution, since slices in this region intersected the fracture surface, and hence are likely to have resulted in VVFs that were artificially low (see argument made in the experimental section regarding slices above fraction metal = 0.5 point).

Fig. 12 gives more detail as to how the particular VVF profiles varied between the cores examined, and also includes an indication of how the size of void changed with distance to the fracture surface. There is a marked difference in void distributions between the separate cores. In the $x = 0.5$ and $x = 1$ mm cores, the voids are concentrated within 500 μm of the surface, but this is less pronounced in the $x = 2$ mm and $x = 4$ mm cores, and the spatial distribution in the $x = 3$ mm core is relatively uniform. This is also borne out in plots of intervoid distance (measured from void centre) vs. fracture surface, Fig. 13, which show more clustering

near the fracture surface in the $x = 0.5$ and $x = 1$ mm cores. The distribution of larger voids is more uniform in the $x = 3$ mm and $x = 4$ mm cores, but in the $x = 0.5$ mm and $x = 1$ mm cores the largest voids appear close to the fracture surface. Indeed, there are voids that are relatively large in size, close to the fracture surface and within 50 μm of each other that do not appear to have coalesced. One would expect to see fewer larger voids with higher spacings if significant coalescence had occurred.

A quantitative comparison of the volume of the inclusions and the volume of their initiating voids was performed using the PFIB data. The comparison in Fig. 14 shows a non-linear correlation, with void size being approximately proportional to inclusion size raised to the power $\approx 3/2$. The voids examined were the IIVs highlighted in Fig. 6 (Void 7 was not included, since this was not associated with an inclusion).

4. Discussion

The multi-scale correlative method utilised here is a valuable tool to further develop our understanding of the sequence of events leading to ductile fracture. From the results described above, it is clear that large IIVs found at MnS inclusions are initiated at the early stages of fracture. There was no evidence of any particle cracking during void nucleation and growth – interface decohesion appeared to be the predominant mechanism of local stress relief. There was also an instance (Void 7) in which a

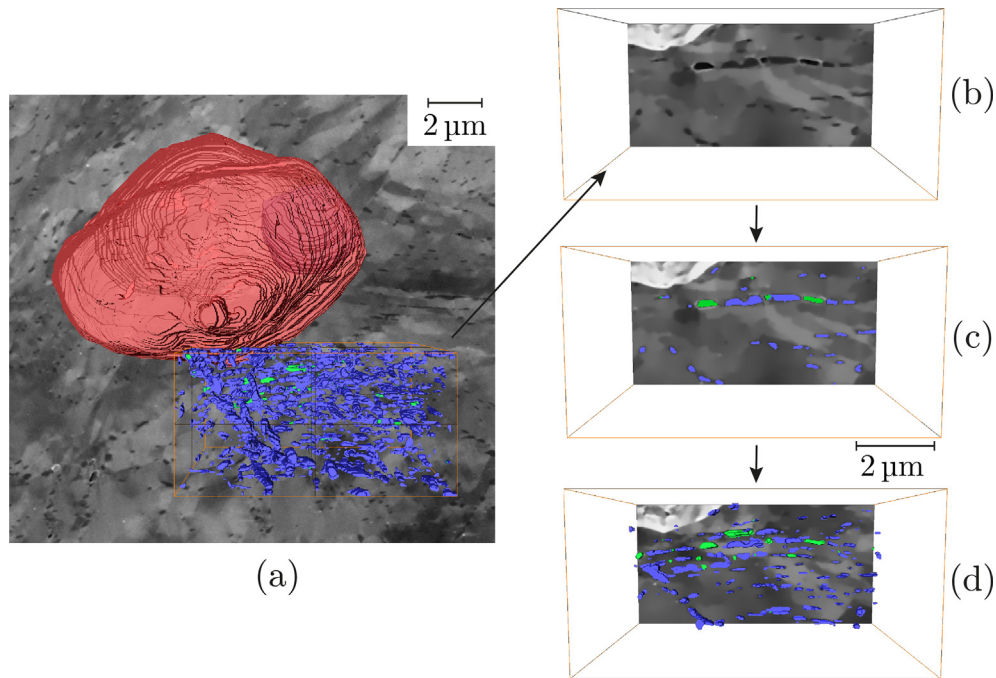


Fig. 9. (a) shows the full volume of Box C, adjacent to Void 2, in which carbides (blue) and associated microvoids (green) are segmented. (b) and (c) show the PFIB TLD image and segmented data for a single slice within Box C, respectively, illustrating the carbide/microvoid interaction in the microstructure. (d) shows a thin stack of images of segmented voids and carbides within Box C. The loading direction was left \leftrightarrow right. (For interpretation of the references to colour in this figure legend, the reader is referred to the web version of this article.)

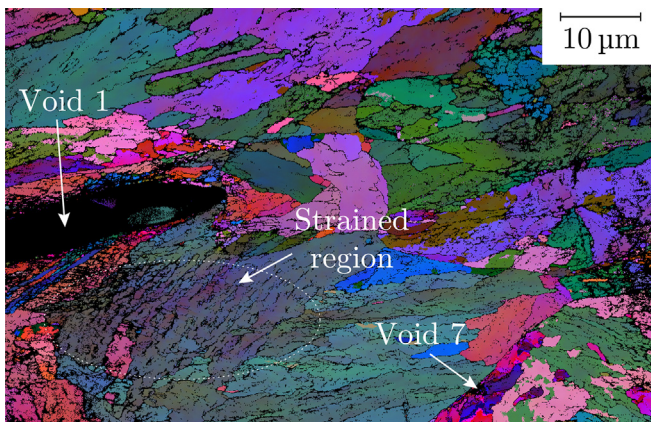


Fig. 10. Grain map (coloured by Euler angle) of region around Voids 1 and 7. An area of strain adjacent to Void 1 is indicated. CIVs were found to exist in this area, akin to Fig. 8. The loading direction was left \leftrightarrow right. (For interpretation of the references to colour in this figure legend, the reader is referred to the web version of this article.)

grain-boundary void was found without detecting an associated particle. Further evidence demonstrating this type of internal decohesion would challenge the commonly-held perception that void formation during ductile tearing occurs exclusively at particles. The damage associated with ductile fracture in the cores extended to depths in excess of 3.5 mm, and was most concentrated within 500 μm of the fracture surfaces of each core. Quantitative results demonstrated significant variations in void sizes and distributions from core-to-core, Figs. 12 and 13, indicating that the results of a single small volume (of the size of the cores examined here) cannot be generalised to represent the behaviour of the bulk material. It was found that the volumes of IIVs scaled with the volumes of their initiating inclusions with a

power law relationship in a region with approximately the same stress intensity (the PFIB VOI), Fig. 14, although a limited number of voids were assessed in the detail required for this analysis (and all were at a similar depth below the fracture surface). Further confirmation of this trend is needed through more serial-sectioning investigations.

The imaging of small CIVs by the multi-scale approach has enabled new insights into their formation behaviour. Our results suggest that they first begin to develop in the material surrounding IIVs, and that they do so along particular directions in the microstructure that are favourable in terms of microstructure and plastic strain, see Fig. 8. No microcracking adjacent to IIVs or CIVs was observed in the regions explored. It is clear that the conditions required to form sheets of CIVs are met at a later stage than those required to initiate IIVs millimetres below the fracture surface, although they are still observed some distance from the surface – the PFIB VOI sat $\approx 400 \mu\text{m}$ from the surface (point where fraction metal = 0.5). It would be useful to understand more fully how the spatial and size distributions of inclusions determine the evolution of damage, in particular the formation of CIVs. Indeed, interest in the mechanics of the CIV sheet formation is likely to increase as steel cleanliness improves and populations of large inclusions are reduced.

The quantitative results provided by the multi-scale analysis should be well-suited to aid the setting of parameters in ductile failure models, such as in the GTN model introduced above. From the VVF information shown in Fig. 11, it can be envisaged that values for the parameters f_0, f_c, f_f, f_N can all be determined in a more direct way. For instance, in the past f_0 has been determined through iterative methods [21,23,30–33], as well as through use of experimental approximations of the volume fraction of non-metallic inclusions [34–37], or by using the Franklin formula [38], which gives an estimated fraction using the weight percent of manganese (C_{Mn}) and sulfur (C_S) measured in the material:

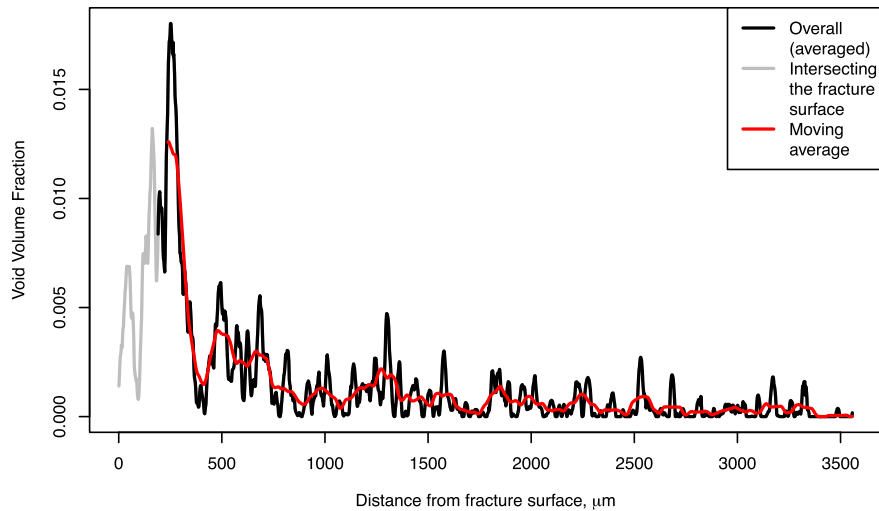


Fig. 11. Void volume fraction as a function of distance below the fracture surface (taken to be where fraction metal = 0.5), obtained from the coarser medium-resolution X-ray CT data (average across all cores). The greyed line represents where the sampled slices intersected the fracture surface in one or more of the cores. The red line is a moving average taken over 100 μm , which ignores the slices intersecting the fracture surface. (For interpretation of the references to colour in this figure legend, the reader is referred to the web version of this article.)

$$f_0 = 0.054 \left(C_S - \frac{0.001}{C_{Mn}} \right) \quad (6)$$

The critical assumption in using the Franklin formula or measured particle fractions is that all inclusions have pre-existing voids associated with them from previous material processing. However, the X-ray CT techniques used in this study detected no voids in the specimen before testing (note: these results are not presented above), suggesting that f_0 should be set to 0. Some particle-like features were detected, but these were assumed to be inclusions. Inclusions were certainly present in the material, and there was no evidence of features with reduced X-ray absorption (in comparison to the features suspected to be inclusions) that would have been indicative of voids, cf. Fig. 4. It should be acknowledged that it is possible that any pre-existing voids were too small to be detected using the high-resolution CT.

At present, there are no rigorous procedures by which values for f_c , f_F and f_N are to be set using datasets like those obtained in this study. As a starting point, we can suggest the following: the value of f_c , the critical VVF for void coalescence, should be set as the final VVF value measured in the moving average data. This approach assumes that the voids directly adjacent to the fracture surface are on the point of coalescing, and do not grow any further as the voids above them are coalescing. The limited evidence found for void coalescence in the cores analysed supports this assumption. In using the moving average data, we are also assuming that 100 μm depth over which the data is averaged is a suitably representative of a 'local' region of uniform, but distinct, behaviour (see discussion below). In this case, the value corresponds to ≈ 0.013 , which is lower than the majority of f_c values used by others [25]. For the value of f_F , we suggest extrapolating the 100 μm moving average curve to the fracture surface (where fraction of metal = 0.5). Here, this was achieved simply by linearly extrapolating the curve in Fig. 11 between 240 and 400 μm (i.e., in the final steep section adjacent to the fracture surface), which gave $f_F \approx 0.034$. There are certainly arguments that the extrapolation method should be more elaborate, perhaps following the plastic strain expected with depth, but it is unclear which particular relationship would be the most appropriate to use at present.

The remaining quantity, f_N , the volume fraction of nucleating

particles, is not easy to ascertain. We could take the VVF in the slices containing the PFIB data and use the relationship plotted in Fig. 14 to extrapolate the total VVF in this region to a total inclusion volume. However, this utilises only a small number of data points at a particular stress state, and also cannot be relied upon to account for *all* the inclusions in the region (since a certain subset will not have formed voids). High-resolution scans are able to find inclusions, as in Fig. 4, and would be most suited to this task. However, there is still a large degree of ambiguity associated with inclusion detection – inclusions can vary in composition and this may effect whether they are detectable or not. The small degree of contrast associated with most inclusions would likely limit the analysis to larger particles only. Hyperspectral imaging may offer an attractive solution in the near future [39], but limited resolution of the technique makes it impractical for the statistical analysis required at present. In light of these considerations, using the Franklin formula might be the best substitute at present. For the SA508 Grade 3 used here, the formula gives an upper limit of 0.0002 for f_N .

The suitability of using 100 μm as a length scale over which to average results deserves some discussion here. This essentially defines the 'local' region ahead of the crack tip that the GTN model is concerned with, and is usually used to set the FEM mesh size used for model implementation. The local region necessarily contains at least two voids that grow and eventually coalesce, and hence its minimum dimension should be the inter-void spacing after void initiation. This value was found from the data in Fig. 13 by assuming that initiation was completed before the increasing in VVF at 500 μm from the fracture surface, and was taken as the approximate void-to-void distance between 500 and 1500 μm from the fracture surface.

In using the Gurson model, we assume that the accumulation of damage at a point is determined solely by the history of plastic strain at that point. This assumption allows us to equate the change in damage we observe with depth below the fracture surface to the change in damage at a point in front of the crack over time, since the same plastic strain is observed, Fig. 15. Therefore, there is a strong argument that the most appropriate way to have plotted the data above would have been against equivalent plastic strain, rather than distance from the fracture surface. However, FE modelling

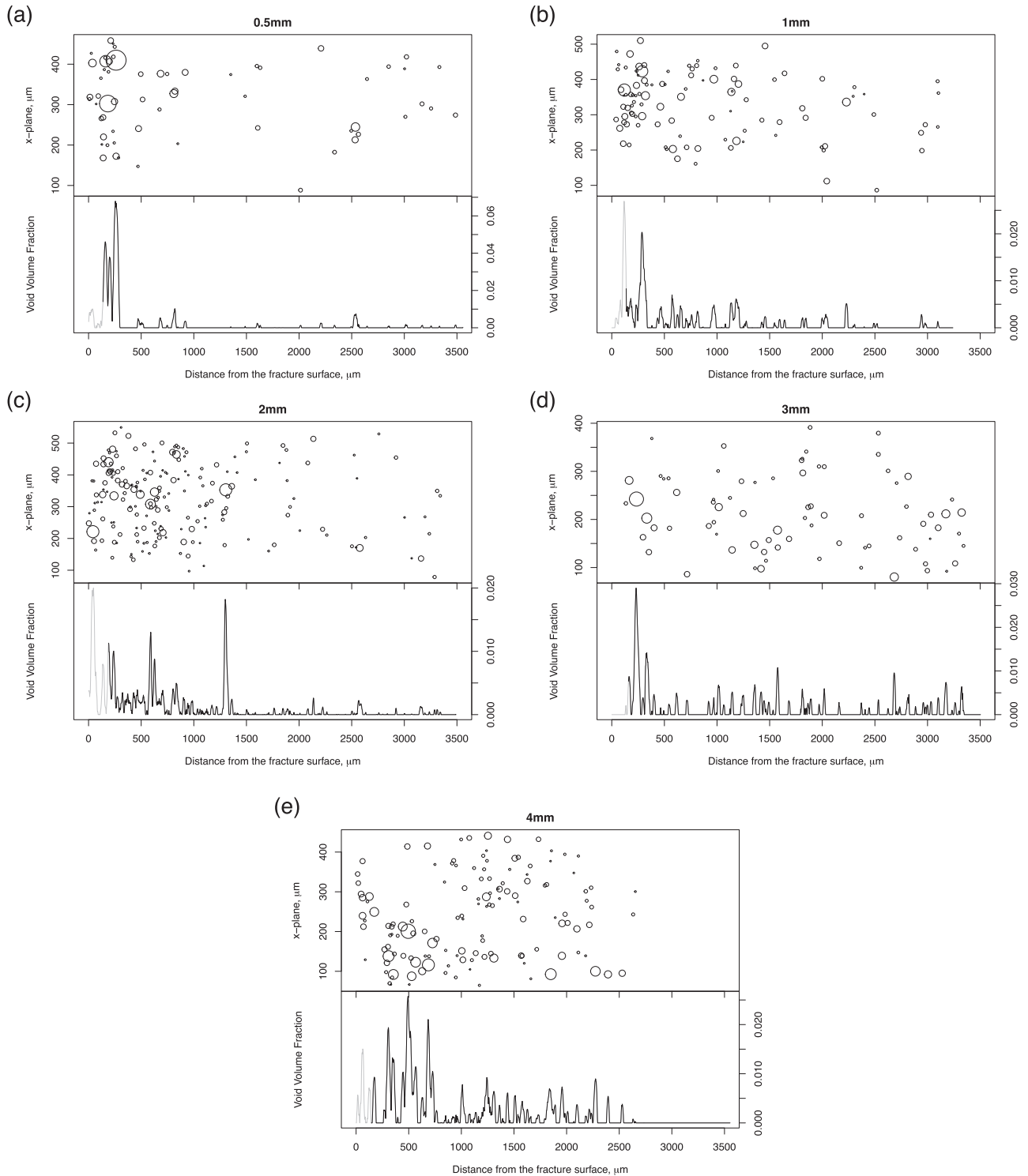


Fig. 12. Plots of VVF as a function of distance below the fracture surface (taken to be where fraction metal = 0.5) for cores at (a) $x = 0.5$ mm, (b) $x = 1$ mm, (c) $x = 2$ mm, (d) $x = 3$ mm and (e) $x = 4$ mm from the notch, obtained from the coarser medium-resolution X-ray CT data, and associated spatial distribution plots. The greyed lines in the VVF plots represent where the sampled slices intersected the fracture surface in the core. In the spatial distribution plots, the sizes of the circles representing each of the voids measured are not to scale, but can be used for a relative comparison. It is evident that VVF seen in the core $x = 0.5$ mm from the notch close to the fracture surface is significantly higher than for the other cores.

would have been required to achieve this, and this was not within the scope of the work presented here.

It is questionable whether the data for the core at $x = 0.5$ mm from the notch, which exhibited significantly higher VVF values

than the other cores, should have been used during the GTN parameter calibration specified above. The increased voiding in this core may have been due to the presence of an 'overloaded' region close to the notch of the CT specimen, as indicated in Fig. 15. The

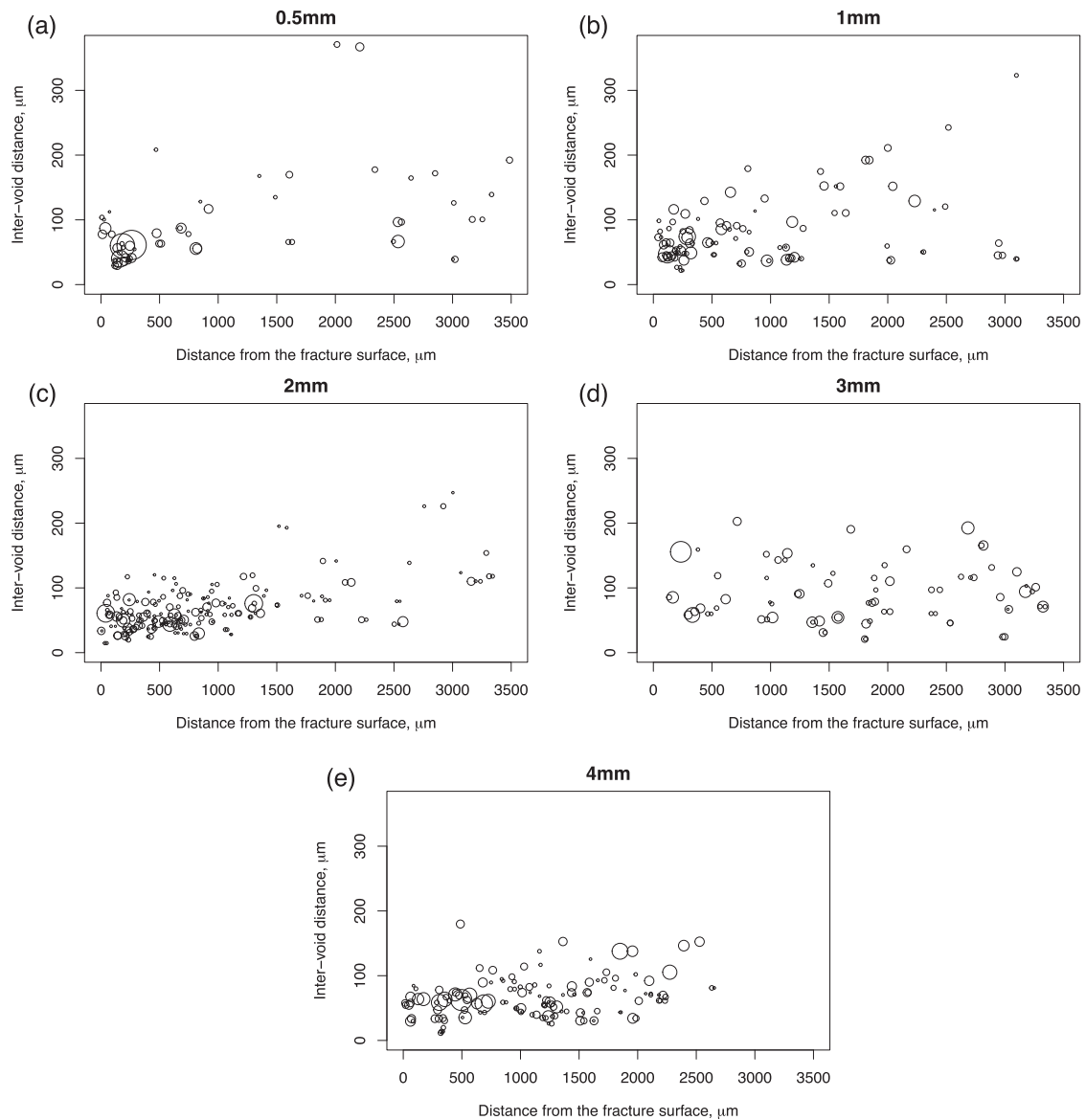


Fig. 13. Plots of intervoid distance vs. distance from fracture surface (fraction metal = 0.5) using medium-resolution data for cores at (a) $x = 0.5$ mm, (b) $x = 1$ mm, (c) $x = 2$ mm, (d) $x = 3$ mm and (e) $x = 4$ mm from the notch. The sizes of the circles representing each of the voids measured are not to scale, but can be used for a relative comparison.

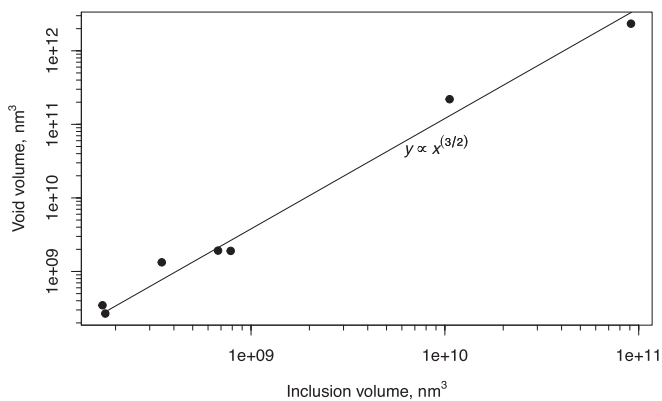


Fig. 14. Comparison of the individual volumes of each void and the volume of their associated inclusion. From the PFIB VOI only (Box A).

initial sharp fatigue crack would have been blunted at the start of testing, and an increased load would have been required to form a sharp crack again. However, this hypothesis cannot be ratified by the results of one core alone, particularly given the random nature of void formation and sampling, and hence the $x = 0.5$ mm core data was retained. Further investigation is needed to confirm whether there is evidence of different voiding behaviour in this ‘overloaded’ region.

The power of the correlative approach employed here lies not only in its capability to characterise features across the length scales with complementary analysis techniques, but also in the high degree of confidence that is associated with its results. For instance, the features in the X-ray CT data that were assumed to be voids could have in fact been regions consisting of a material with a lower electron density than the surrounding matrix. By examining these features with PFIB sectioning, direct evidence was provided that they were voids and not any other type of defect. Cross-dataset

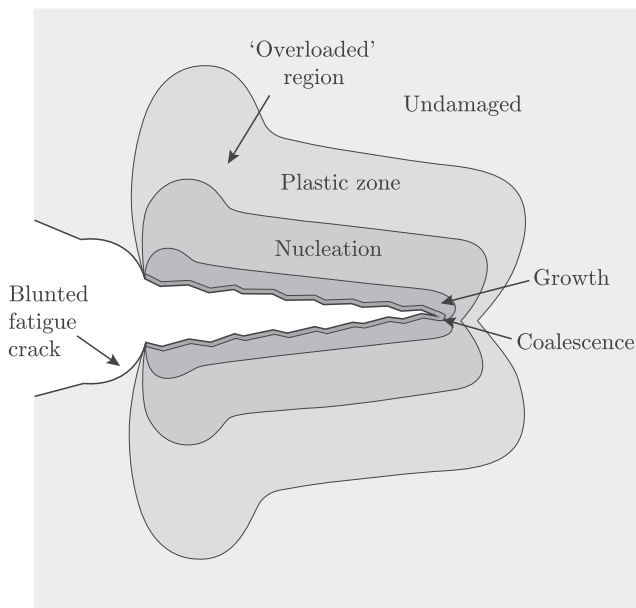


Fig. 15. Schematic showing the regions of damage generated during ductile fracture. Regions in which void nucleation, growth and coalescence occur are distinguished. Note that the relative scales of each of the regions are not accurate. The crack is propagating left-to-right.

comparisons of this type can eradicate the ambiguities that can plague simpler identification procedures. Another key advantage of the multiscale approach used here is that it is able to probe fine-scale features, whilst also retaining the mechanical test conditions experienced in large components. By extracting cores from full-scale test rather than conducting small-scale tests, the results from testing under high levels of constraint can be examined.

In reality, the tearing behaviour of a material must be a function not only of total VVF, but also the size and spatial distributions of the voids [14]. Even more complexity is likely to be associated with the shape and orientation of void-nucleating particles [14,15], and these factors are not accounted for in the GTN model. However, this type of information can be harvested using the multiscale approach detailed here, and it is hoped that future analyses will highlight the significance of these effects.

This study has been concerned principally with assessing the void damage induced by a running sharp tearing crack. In order to complete the experimental characterisation of the damage induced during a compact tension test, two further states of damage should be investigated in the future: (i) the damage ahead of the blunted fatigue pre-rack crack tip prior to the formation (initiation) of a propagating sharper crack, and (ii) the damage present in front of the sharp tearing crack front at the end of the test. Such results could then be used to feed an advanced 3D model of a compact tension test, which would provide a preliminary comparison between experimental void measures and continuum measures of local stress and strain.

5. Conclusions

A multi-scale correlative technique involving the successive use of 3D X-ray tomography and plasma focussed-ion beam (PFIB) analyses was used to investigate the ductile fracture in SA508 Grade 3 pressure vessel steel. The techniques utilised were able to characterise, within the same material volume, large voids associated with large inclusions (IIVs), as well as the fine voids nucleated at

carbides (CIVs). It is now possible for us to gain further insight into the important role that these small voids are thought to play during ductile failure of steels.

It was found that the volumes of IIVs varied according to the volume of their initiating inclusions raised to the power $3/2$, emphasising the importance of inclusion size distribution, as well as their volume fraction. Further confirmation of this trend is needed, however. The most severe voiding was concentrated within $500\ \mu\text{m}$ of the fracture surface, but measurable damage was found to extend to a depth of at least $3\ \text{mm}$.

CIVs were observed to nucleate in particular regions adjacent to IIVs that were associated with high levels of plastic strain. These localised populations of CIVs presumably act as precursors to the formation of the void sheets that lead ultimately to failure. They were observed at depths of at least $400\ \mu\text{m}$ from the fracture surface.

The information gleaned from multi-scale analyses can assist with the calibration of models for ductile fracture, such as the Gurson-Tvergaard Needleman (GTN) model. An initial outline of how data might be used to set particular GTN parameters has been set out, although the procedures by which model parameters can be set using experimental results in a robust fashion require development. It is hoped that multi-scale results can be used to inform models, highlight their deficiencies and improve their formulation.

In general, there is great scope for the application and extension of the multi-scale correlative tomography method used here to explore the features of ductile fracture in even greater detail. Time-lapse X-ray CT could also be used to map the progress of damage in the same specimen, and PFIB-SEM serial sectioning has the potential to explore the nature of the interface between the metal matrix and inclusions using TEM in a further extension of the scales investigated [8]. Indeed, it may be possible to incorporate lab-based grain-orientation mapping into the process [40], such that local crystal plasticity can be accounted for, and complex void distributions like that shown in Fig. 8 predicted. It must be recognised that the complex fine-scale nature of continuously-cooled steel microstructures might make this particularly challenging, and that constraint effects from a large volume of surrounding material will likely have to be accounted for. Nevertheless, the development of multi-scale methods has meant that it is now at least experimentally feasible to embark on such an investigation.

Acknowledgements

The X-ray CT experiments were undertaken within the Henry Mosley X-ray Imaging Facility (HMXIF) at the University of Manchester, established with funding from EPSRC through grants EP/F007906/1, EP/F001452/1 and EP/I02249X/1. The support of an ERC advanced grant for P.J. Withers (CORREL-CT) is gratefully acknowledged. The authors would also like to thank Mr John Sharples and Dr Peter James at Amec Foster Wheeler, UK, for useful technical discussions during the course of this work. The raw X-ray CT and PFIB data files gathered in this work can be accessed here: DOI [10.5281/zenodo.238854](https://doi.org/10.5281/zenodo.238854).

References

- [1] S.R. Stock, Recent advances in X-ray microtomography applied to materials, *Int. Mater. Rev.* 53 (2008) 129–181.
- [2] E. Maire, P.J. Withers, Quantitative X-ray tomography, *Int. Mater. Rev.* 59 (2014) 1–43.
- [3] E. Maire, S. Zhou, J. Adrien, M. Dimichiel, Damage quantification in aluminium alloys using in situ tensile tests in X-ray tomography, *Eng. Fract. Mech.* 78 (2011) 2679–2690.
- [4] M. Daly, F. Leonard, A. Sherry, Application of 3D X-ray tomography to enhance the calibration of ductile fracture models, in: 2014 ASME Pressure Vessels &

- Piping Conference: ASME Pressure Vessels & Piping Conference, 2014, pp. PVP2014–28318.
- [5] C. Schlacher, T. Pelzmann, C. Béal, C. Sommitsch, C. Gupta, H. Toda, P. Mayr, Investigation of creep damage in advanced martensitic chromium steel weldments using synchrotron X-ray micro-tomography and EBSD, *Mater. Sci. Technol.* 31 (2015) 516–521.
 - [6] E. Maire, T. Morgener, C. Landron, J. Adrien, L. Helfen, Bulk evaluation of ductile damage development using high resolution tomography and laminography, *C. R. Phys.* 13 (2012) 328–336.
 - [7] J. Lorthios, F. Nguyen, A.F. Gourgues, T.F. Morgener, P. Cugy, Damage observation in a high-manganese austenitic TWIP steel by synchrotron radiation computed tomography, *Scr. Mater.* 63 (2010) 1220–1223.
 - [8] T.L. Burnett, R. Geurts, H. Jazaeri, S.M. Northover, S.A. McDonald, S.J. Haigh, P.J. Bouchard, P.J. Withers, Multiscale 3D analysis of creep cavities in AISI type 316 stainless steel, *Mater. Sci. Technol.* 31 (2015) 522–534.
 - [9] J. Caplan, M. Niethammer, R.M. Taylor II, K.J. Czymmek, The power of correlative microscopy: multi-modal, multi-scale, multi-dimensional, *Curr. Opin. Struct. Biol.* 21 (2011) 686–693.
 - [10] T.L. Burnett, S.A. McDonald, A. Gholinia, R. Geurts, M. Janus, T. Slater, S.J. Haigh, C. Ornek, F. Almuaili, D.L. Engelberg, G.E. Thompson, P.J. Withers, Correlative tomography, *Sci. Rep.* 4 (2014) 4711.
 - [11] H.C. Rogers, *Transactions of TMS AIME* 218, 1960, pp. 498–506.
 - [12] T.B. Cox, J.R. Low Jr., An investigation of the Plastic Fracture of AISI 4340 and 18 Nickel–200 Grade maraging steels, *Metall. Trans.* (1974) 1457–1470.
 - [13] J.W. Hancock, A.C. Mackenzie, On the mechanisms of ductile failure in high-strength steels subjected to multi-axial stress-states, *J. Mech. Phys. Solids* 24 (1976) 147–169.
 - [14] T. Pardoen, J.W. Hutchinson, An extended model for void growth and coalescence, *J. Mech. Phys. Solids* 48 (2000) 2467–2512.
 - [15] F.M. Beremin, Cavity formation from inclusions in ductile fracture of A508 steel, *Metall. Trans. A* 12 (1981) 723–731.
 - [16] A.L. Gurson, Continuum theory of ductile rupture by void nucleation and growth: Part I—yield criteria and flow rules for porous ductile media, *J. Eng. Mater. Technol.* 99 (1977) 2–15.
 - [17] V. Tvergaard, Influence of voids on shear band instabilities under plane strain conditions, *Int. J. Fract.* 17 (1981) 389–407.
 - [18] V. Tvergaard, On localization in ductile materials containing spherical voids, *Int. J. Fract.* 18 (1982) 237–252.
 - [19] V. Tvergaard, A. Needleman, Analysis of cup-cone fracture in a round tensile bar, *Acta Metall.* 32 (1984) 157–169.
 - [20] C.C. Chu, A. Needleman, Void nucleation effects in biaxially-stretched sheets, *J. Eng. Mater. Technol.* 102 (1980) 249–256.
 - [21] L. Xia, C.F. Shih, J.W. Hutchinson, A computational approach to ductile crack growth under large scale yielding conditions, *J. Mech. Phys. Solids* 43 (1995) 389–413.
 - [22] Z.L. Zhang, E. Niemi, A new failure criterion for the gurson-tvergaard dilatational constitutive model, *Int. J. Fract.* 70 (1995) 321–334.
 - [23] C. Ruggieri, T.L. Panontin, R.H. Dodds Jr., Numerical modeling of ductile crack growth in 3-d using computational cell elements, *Int. J. Fract.* 82 (1996) 67–95.
 - [24] P.F. Thomason, A view on ductile-fracture modelling, *Fatigue Fract. Eng. Mater. Struct.* 21 (1998) 1105–1122.
 - [25] G. Bernauer, W. Brocks, Micro-mechanical modelling of ductile damage and tearing - results of a european numerical round robin, *Fatigue Fract. Eng. Mater. Struct.* 25 (2002) 363–384.
 - [26] N. Benseddiq, A. Imad, A ductile fracture analysis using a local damage model, *Int. J. Press. Vessels Pip.* 85 (2008) 219–227.
 - [27] ASTM, Standard Specification for Quenched and Tempered Vacuum-Treated Cabon and Alloy Steel Forgings for Pressure Vessel Components A508A/A508M, 2004.
 - [28] ESIS TC1 Subcommittee on Fracture Mechanics Testing Standards, ESIS Procedure for Determining the Fracture Behaviour of Materials ESIS P2-92, Tech. Rep, European Structural Integrity Society, 1992.
 - [29] T.L. Burnett, R. Kelley, B. Winiarski, L. Contreras, M. Daly, A. Gholinia, M.G. Burke, P.J. Withers, Large volume serial section tomography by Xe plasma FIB dual beam microscopy, *Ultramicroscopy* 161 (2016) 119–129.
 - [30] L. Xia, C.F. Shih, Ductile crack growth - I. A numerical study using computational cells with microstructurally-based length scales, *J. Mech. Phys. Solids* 43 (1995) 233–259.
 - [31] A. Corigliano, S. Mariani, B. Orsatti, Identification of gurson-tvergaard material model parameters via kalman filtering technique. I. Theory, *Int. J. Fract.* 104 (2000) 349–373.
 - [32] M. Springmann, M. Kuna, Identification of material parameters of the gurson-tvergaard-needleman model by combined experimental and numerical techniques, *Comput. Mater. Sci.* 32 (2005) 544–552.
 - [33] Z. Xue, M.G. Pontin, F.W. Zok, J.W. Hutchinson, Calibration procedures for a computational model of ductile fracture, *Eng. Fract. Mech.* 77 (2010) 492–509.
 - [34] R. Batisse, M. Bethmont, G. Devesa, G. Rousselier, Ductile Fracture of A 508 Cl 3 steel in relation with inclusion content: the benefit of the local approach of fracture and continuum damage mechanics, *Nucl. Eng. Des.* 105 (1987) 113–120.
 - [35] D.Z. Sun, D. Siegel, B. Voss, W. Schmitt, Application of local damage models to the numerical analysis of ductile rupture, *Fatigue Fract. Eng. Mater. Struct.* 12 (1989) 201–212.
 - [36] M. Rakin, Z. Cvijovic, V. Grabulov, M. Kojic, Micromechanism of ductile fracture initiation - void nucleation and growth, *Facta Univ.-series Mech. Eng.* 1 (2000) 825–833.
 - [37] M. Rakin, Z. Cvijovic, V. Grabulov, S. Putic, A. Sedmak, Prediction of ductile fracture initiation using micromechanical analysis, *Eng. Fract. Mech.* 71 (2004) 813–827.
 - [38] A.G. Franklin, Comparison between a quantitative microscope and chemical methods for assessment of non-metallic inclusions, *J. Iron Steel Inst.* 207 (1969) 181–186.
 - [39] C.K. Egan, S.D.M. Jacques, M.D. Wilson, M.C. Veale, P. Seller, A.M. Beale, R.A.D. Patrick, P.J. Withers, R.J. Cernik, 3D chemical imaging in the laboratory by hyperspectral X-ray computed tomography, *Sci. Rep.* 5 (2015) 15979.
 - [40] S.A. McDonald, P. Reischig, C. Holzner, E.M. Lauridsen, P.J. Withers, A.P. Merkle, M. Feser, Non-destructive mapping of grain orientations in 3D by laboratory X-ray microscopy, *Sci. Rep.* 5 (2015) 14665.